npj | materials degradation

Article

Published in partnership with CSCP and USTB

https://doi.org/10.1038/s41529-025-00650-2

Effect of salt deposition patterns on stress corrosion cracking

Check for updates

Mustafa Elsherkisi[1], Fabian Duarte-Martinez[1], Julian Mason-Flucke[2], Simon Gray[1] & Gustavo M. Castelluccio[1] ✉

While substantial research has been devoted to understanding environmental degradation mechanisms in Ni-base superalloys, the influence of solid contamination morphology on cracking remains comparatively underexplored. This study combines computational modeling and experimental approaches to investigate cracking behavior in CMSX-4 single-crystal superalloys exposed to salt deposition patterns in sulfur-rich environments at moderate temperatures. Utilizing phase-field computational models, we develop a digital twin of the experimental setup to examine crack propagation under varying deposition configurations. The findings reveal that salt deposition patterns can inhibit crack shielding, leading to increased crack lengths and shorter fatigue lives. A novel experimental salt configuration resulted in crack lengths extending from 300 μm to over 2 mm under static loading conditions and decreased corrosion-fatigue life by as much as 83%. The results demonstrate that modeling is a valuable tool to mitigate experimental uncertainty.

Stress corrosion cracking (SCC) is a leading failure mechanism in metallic material across myriads of industries, and it can result in catastrophic damage with significant human and economic losses[1]. Thus, understanding and mitigating the mechanisms and conditions that promote SCC is a requirement for component certification. Engineers have addressed this need through extensive experimental testing, which often carries uncertainty in their approximation of the realistic environment experienced by components during service. Standardization bodies have contributed with assessment approaches that evaluate crack initiation with convenient self-loaded samples (e.g., C-ring testings ISO 7539-5[2] and ASTM G38[3]), which are preloaded before being exposed to detrimental environments. For example, ASTM has standardized SCC assessment of 2XXX and 7XXX Aluminum series[4] through testing samples in 3.5 wt% NaCl aqueous solution, which accelerates materials degradation. Similarly, SCC induced by gaseous contamination can be tested with more complex environmental chambers[5].

Nonetheless, many industrial components such as steam and gas turbines[6], offshore wind turbines[7], and sub-sea piping[8] often experience SCC initiation from solid particle contamination coupled with gaseous or aqueous environments. In these cases, testing protocols are less understood and not standardized. For example, researchers have assessed materials degradation by contaminating surfaces with salt solutions[9], which drastically promotes SCC mechanisms. Multiple studies[10–12] have followed a similar approach by coating samples with different salt compounds and different ambient conditions. However, very few studies assessed the role of the salt deposition patterns on crack initiation and propagation. Mi et al.[13] adopted inkjet printing to deposit different MgCl salt deposition patterns on 304 stainless steel specimens, and found that the diameter of pits increased as the original salt deposition diameter increased. He et al.[14] found similar results when investigating the role of droplet size on the localized corrosion of M50-bearing steel when exposed to salt water-contaminated lubricant oil. These results suggest that the size and morphology of contaminants affect the degradation and increase prognosis uncertainty extrapolated from laboratory experiments.

In the case of gas turbines, sand and other debris are regularly absorbed and transmitted through the cooling systems and combustion chamber. Salt deposition on surfaces can induce mechanical or corrosion damage, which is aided by high temperatures and a corrosive atmosphere. Several studies[15] have shown that salts combined with specific gaseous contaminants accelerate SSC drastically. For example, Fig. 1, obtained during our prior experiments[15], presents a high density of crack embryos initiated from the remains of salt contamination. Interestingly, cracks have regular lengths and spacing, which has been explained[16] as the result of crack interference. Prior work with phase-field modeling (PFM)[16] explained crack stagnation despite their continuous exposition to conditions that promote SCC. The analysis pointed to crack interaction mechanisms, which can prematurely halt or accelerate due to crack shielding or coalescence, respectively. Shielding effects reduce crack growth by locally reducing crack tip stresses, while crack coalescence promotes growth by merging crack tips[17]. However, only established crack embryos were considered using predefined cracks, and the role of the contamination pattern in interacting with the cracking has not been explored.

This study integrates experiments and models into a digital twin framework to investigate the influence of salt contamination pattern, density, and dispersion on SCC in single-crystal nickel-based superalloys at 550 °C. A PFM simulates corrosion-induced damage to demonstrate that crack length scales are controlled by the pattern of the contaminant salt. By systematically varying the contamination pattern, we assess different cracking responses, which can be modulated to either enhance or suppress interaction mechanisms. These

[1]School of Aerospace, Transport and Manufacturing, Cranfield University, Bedfordshire, UK. [2]Rolls-Royce Plc, Bristol, UK. ✉e-mail: castellg@cranfield.ac.uk

outcomes can then inform the design of novel experimental protocols, with the goal of assessing component failure under the most detrimental SCC conditions, thereby revealing the previously unrecognized dominant role of contamination patterns in SCC testing environments.

Results and discussion

2D salt pattern modeling

Computational models excel at integrating limited knowledge into digital twins that optimize testing protocols by propagating uncertainty. Hence, prior to running new experiments, we assessed the effects of the contamination pattern with a PFM in which contaminants are localized in different arrangements, as shown in Fig. 2. The analysis employs a 1500 × 1500 μm 2D model in which salt is localized in a grid within an 800 × 800 μm area using one, four, nine, and 16 depositions regularly aligned (Fig. 2a, b, c, d, respectively). This configuration follows the premise that a crack will initiate underneath the halo of each salt deposition, as demonstrated by previous studies[5]. The model is pinned from the nodes along the bottom (UX=UY=0) while a displacement of 0.2625 mm is applied along the top nodes; the side displacement is restricted in the X direction (UX = 0) to produce a uniform stress of ~700 MPa. An impurity concentration of 0.5 wppm is applied to the nodes at the deposition site, and the model uses the diffusion coefficient matching that of sulfur in nickel (at 600 °C[18]). These simple simulations had a running time of just a few minutes on a conventional computer.

Figure 3 presents the results of this analysis with the colorbar indicating the phase field parameter, ϕ, which runs on a scale from 0 (undamaged material) to 1 (completely degraded material). Figure 3a demonstrates that a

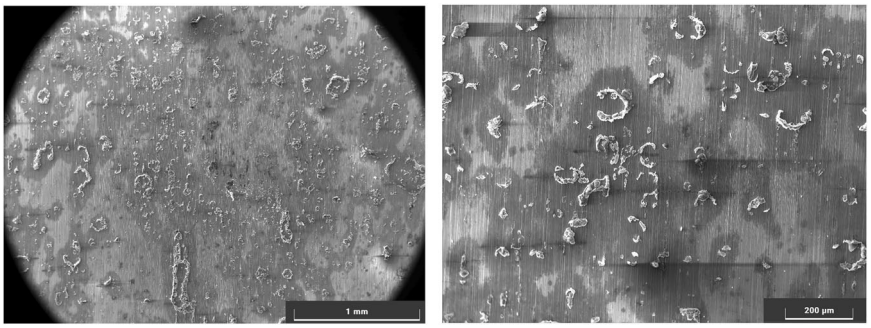


Fig. 1 | SEM examples of salt deposition sites highlighting the random nature of the process. The experimental procedure corresponds to that detailed in ref. 15.

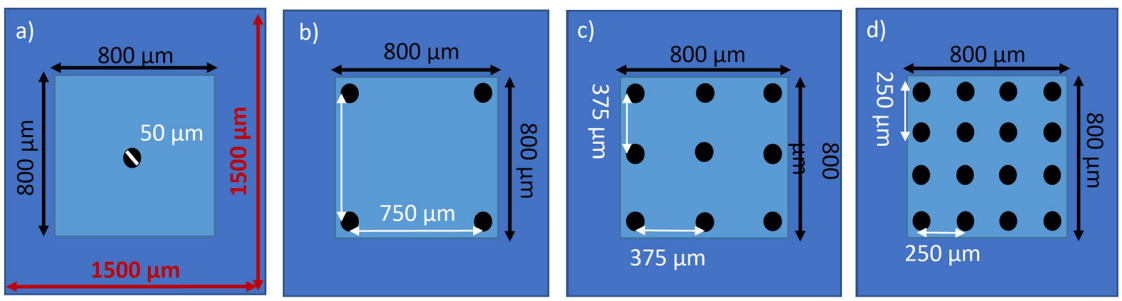
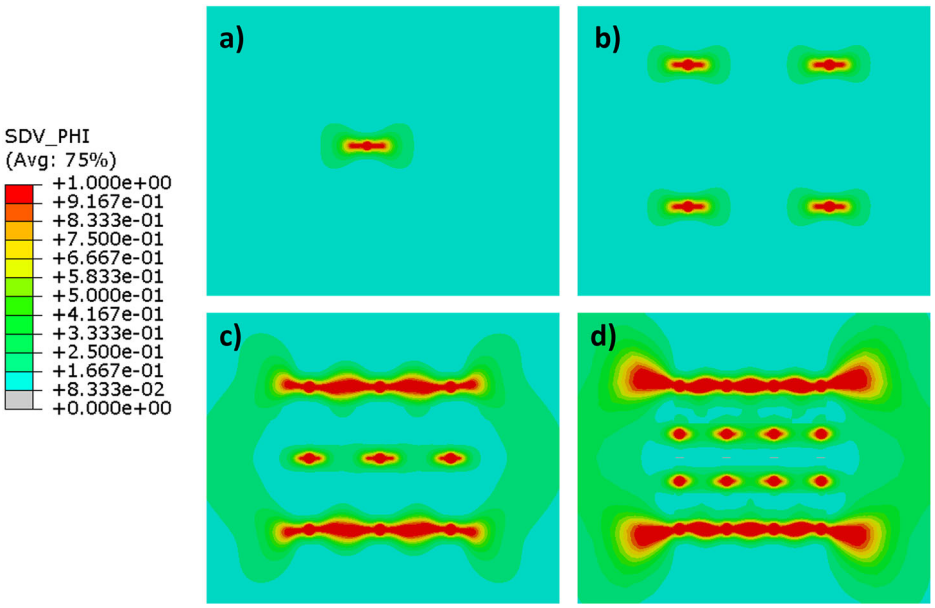


Fig. 2 | Schematic for the 2D simulations used to understand how the spacing between salt deposition sites may result in shorter or longer cracks. a-d Correspond to 1, 4, 9, and 16 salt deposition sites, respectively, in an array configuration.

Fig. 3 | Final crack formation as a result of crack interaction mechanisms, or lack thereof. **a-d** Correspond to the cracking outcome of 1, 4, 9, and 16 salt deposition sites respectively. All four cases had a test time of 1-hour.



crack initiates and propagates freely from a single deposition site. Hence, if sufficient corrosive species and stress are available, the simulations predict that a crack will grow unbound until reaching the boundary.

When the number of salt sites is increased to four sites, the spacing between the sites is sufficient for the cracks to grow to the same lengths as those seen for a single deposition after a similar exposure time. However, for 9 and 16 salt deposition sites, the external cracks (for both at the top and bottom) coalesced into seemingly two long cracks, arresting the central cracks. In this case, the separation distance is short enough such that the surrounding cracks promote stress shielding on the central sites by locally reducing the crack tip stress. A stress below the critical threshold of SCC naturally arrests the process[19]. Hence, this simple simulation demonstrates that the deposition pattern can play a role in the crack distributions and morphologies.

The salt spray deposition method used to produce the sample shown in Fig. 1 results in clusterings of salt particles with regular patterns. Hence, Fig. 3 suggests that such a salt pattern can significantly affect cracking behavior. Similarly, other factors, such as the amount of salt flux, may also prove significant. If the volume of the salt solution remains constant but the salt flux is increased, it has the potential to change the density and concentration of the pattern, which may appear to be more harmful. However, if the salt flux is reduced, then fewer salt depositions will likely be seen for the same area, and hence the chances of fewer, but longer, cracks occurring because of a lack of shielding are probable. Counterintuitively, this analysis suggests that lower salt flux has the potential to cause more catastrophic cracking. Both high and low salt flux conditions have the potential to be detrimental, but further testing across multiple materials, test conditions, and repeated trials is necessary to confirm these findings.

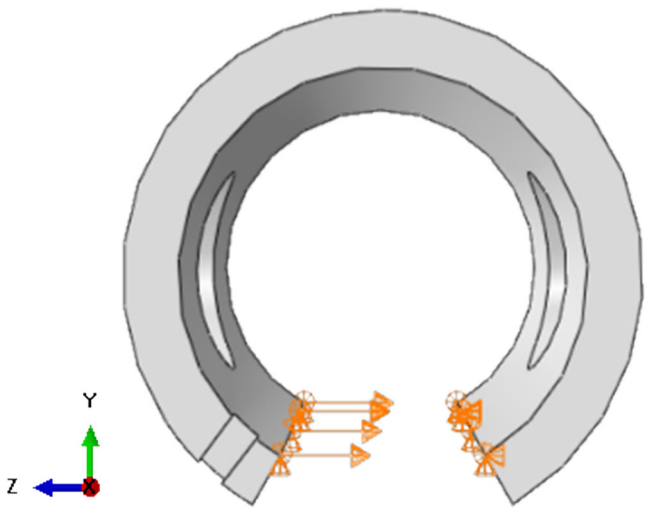


Fig. 4 | Schematic to represent how the boundary conditions are applied to the C-ring geometries. Triangles represent a pinned boundary condition, while arrows correspond to the applied displacement.

3D C-ring modeling

Next, we explore 3D modeling of C-rings (Fig. 4), which are often employed to assess SCC experimentally. Boundary conditions replicate the tensile stress produced by the bolt through the hole by pinning one side of the C-ring from the bottom ridge (i.e., UX = UY = UZ = 0) and sufficiently displacing the other side (in the *Z*-direction) up to a peak stress of 700 MPa along the apex. Since this stress is below the yield, plastic strains are only seen on a small scale in the vicinity of the hole with no significant impact on cracking, as demonstrated by J2 plasticity modeling in Abaqus; these models have proprietary data, and the results cannot be included. As such, the additional complexity associated with introducing extended plasticity was deemed unjustified, and an elastic approach was adopted. Creep effects can also be neglected in both physical and computational testing, as the temperatures of interest are below those typically associated with dominant creep deformation for the material used.

The C-ring model contains a predefined crack (400 × 250 μm) in the center of the sample apex with a constant salt concentration boundary during 50 h of exposure. The simulations employ cubic anisotropic crystal elasticity, which matches the orientation of the crystals in the experiments. Figure 5 presents the modeling results and demonstrates that a singular deposition site can reach a total predicted crack length of 2 mm if allowed to grow unbounded under experimental conditions. However, images from C-ring testing (Fig. 1) present crack lengths in the range of 20–300 μm, which is an order of magnitude smaller than those predicted for equivalent testing time. This difference suggests that if cracks were allowed to grow without interference, the outcome would be more detrimental than in the current testing results. Next, we leverage on modeling results to explore testing configurations that can result in more detrimental outcomes.

PFM modeling[16] has accurately captured shielding and coalescence crack effects, which suggests that the discrepancies in crack lengths between models (Fig. 5) and experiments (Fig. 1) result from different crack geometry configurations. More importantly, this analysis highlights that some configurations can be significantly more detrimental than those tests with crack lengths much longer than those observed in experiments. Hence, we propose novel experimental protocols with different salt patterns aimed at isolating cracks.

'Zebra' C-ring pattern

The first experiment redesign is named "Zebra" and corresponds to a C-ring sample with portions of the surface taped off before being sprayed with 1.2 μg/cm^2/h of NaCl, as shown in Fig. 6. After removing the tape, some areas are salt-free with a straight interface separating salted/unsalted substrate. Figure 7a, b presents the pattern of salt deposition on a pre- and post-exposed C-ring, respectively. This experiment has five salted interfaces, so multiple crack initiation sites can develop independently to study the repeatability of the cracking process. The Zebra specimen was exposed to the same experimental conditions as in our prior efforts[15] (i.e., crystal

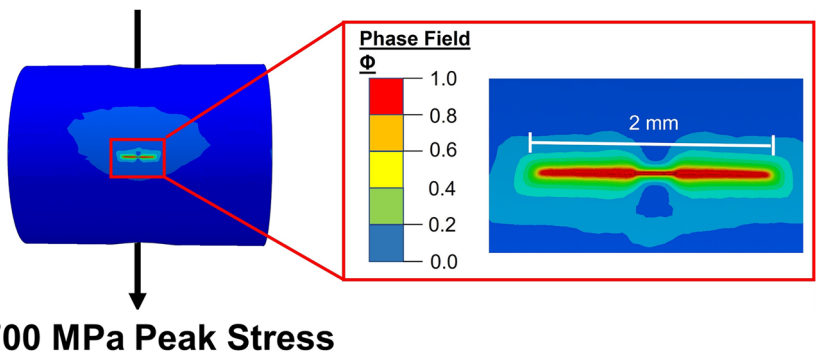


Fig. 5 | Phase field modeling results for crack growth from a single salt deposition site. The simulation corresponds to a testing time of 50 h.

orientation, displacement, salt concentration, 550 °C for 50 h, etc[16]) with the only difference being the salt deposition coverage limited to stripes.

Figure 8 presents SEM images of the Zebra sample after testing. The unsalted section presents no cracks, while the salted region depicts crack shielding as evidenced before, with typical crack lengths of 200 µm. However, the interface between the salted/unsalted resulted in crack lengths between 500 µm and 1 mm, which span mostly into the unsalted area. Over ten cracks were observed at the interfaces, all similar in nature. These interface cracks are about three times longer than previously seen in any fully salted C-ring tests[5], which demonstrates that cracks have grown unbounded. Thus, cracking strongly depends on the contamination pattern.

Notably, cracks on the salted Zebra interfaces were separated by a strikingly regular spacing of about 200 µm (Fig. 8A, B), agreeing with the minimum distance previously predicted to avoid crack shielding[16]. The Zebra setup also shows that the contaminant diffusion plays a significant role in the propagation, showing limited propagation beyond the salt boundary (Figs. 8C, 9). This diffusion length scale likely depends on the deposition method, salt solution concentration, and environmental temperature.

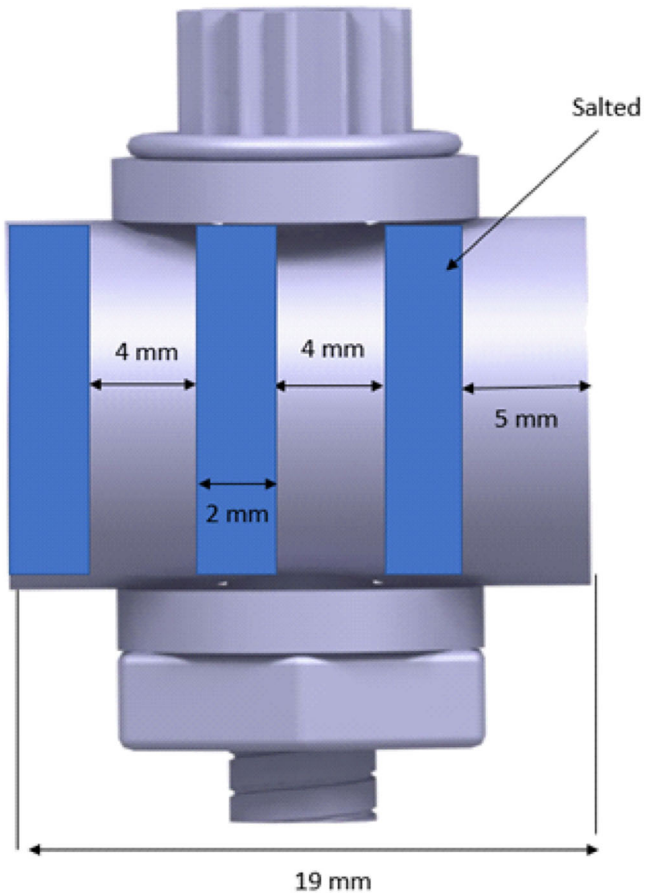


Fig. 6 | Zebra C-ring testing—schematic representation of the novel experimental configuration, designed to modify crack shielding. Shielding still occurs on the stripes, but not in between. Note the spacing between salted and unsalted regions.

Figure 10 presents a back-scattered electron image of a cross-section with some cracks present. This image clearly shows multiple cracks propagating well into the depth of the material, confirming that the cracking is not confined to the surface but extends through the thickness. Figure 11 compares the number and depth of cracks observed in cross-sections from both the salted region ("b") and the non-salted region ("d"), though it is noted that some salt contamination is likely to have diffused to the "d" samples. The salted region exhibits not only a higher number of cracks but also greater average crack depths. The comparison of these cracks is not straightforward, since no cracks nucleate in the unsalted area and cracking in the unsalted area may correspond to the edges of a crack initiated in the salted area (so shorter). Furthermore, C-rings have a typical section width of about 1.6 mm, and they undergo a bending stress imposed by the bolt. Such a thin section results in a strong stress gradient, so the cracking driving force reduces rapidly as it grows away from the surface. Therefore, surface cracking becomes prevalent, and cracks are more superficial in nature. These findings complement the understanding and support that the contaminant pattern affects the crack morphology.

"One-dot" C-ring pattern

The Zebra samples demonstrated that the contaminant diffusion length scale is larger than the stress influence field, and hence it does not control the crack typical length scale of 400 µm. Hence, we designed the so-called "Dot" contamination pattern, which intends to deposit a single drop of contaminant of about 200 µm in radius. This size assumes that sprayed salt results in a single crack within a spacing of about 400 µm, so a deposition about this size or smaller will only be able to initiate a single crack, avoiding shielding effects.

The traditional methodology for spray salt was replaced by deposition with a micropipette, placing three droplets of salt solution spaced by 5 mm on the surface of the CMSX-4 C-ring after exposure to a hot plate. However, unlike our previous work, the salt flux levels were varied to understand the role of salt boundary dispersion. The first droplet used a standard 1.2 µg/cm^2/h, while the remaining have twice and four times the values. All other experimental parameters remained similar to previous C-ring tests (i.e., bolt displacements 0.42 mm at 550 °C, total duration of 50 h).

Figure 12 depicts an optical microscopy image before testing and demonstrates that a higher salt flux results in a slightly smaller salted area. We regard this effect as caused by a smaller initial droplet as a result of a higher surface tension effect or reduced water concentration. Certainly, a higher surface tension resists droplet spreading, causing the solution to bead up and deposit salt over a smaller, more concentrated area upon drying. Optical images in Fig. 13 show the extent of cracking after exposing the sample for 50 h at 550 °C. Figure 13b corresponds to a deposition with the same salt concentration as previous C-ring experiments and resulted in a total crack length of 1.61 mm, which is five times longer than those cracks from spraying salt, and twice the length in the Zebra specimen.

The results also seem to suggest that a higher flux could generally promote longer cracks by allowing further diffusion of contaminant in unshielded cracks. This idea can be further supported by Fig. 14, which

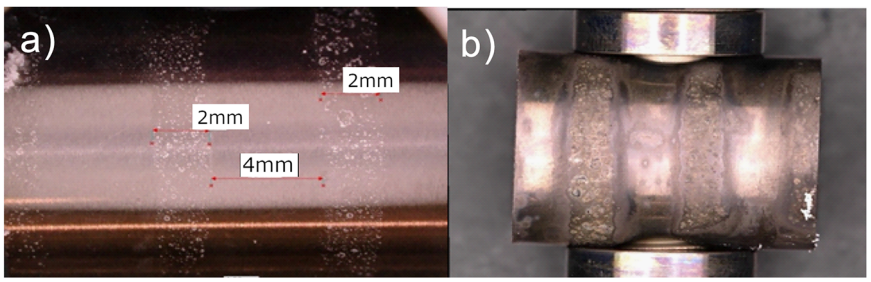
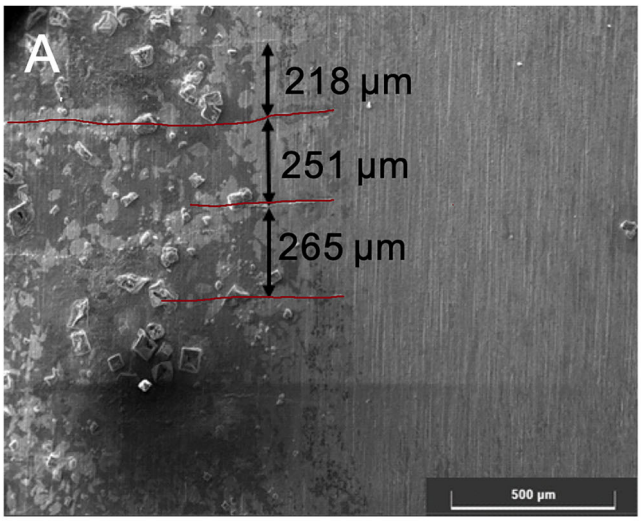
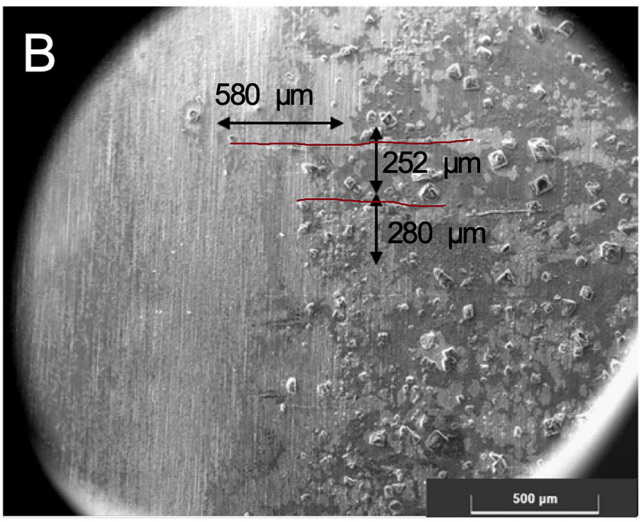


Fig. 7 | Optical images of the Zebra specimens. **a** Distribution of salt deposited pre-testing and **b** Post-exposed Zebra C-ring.





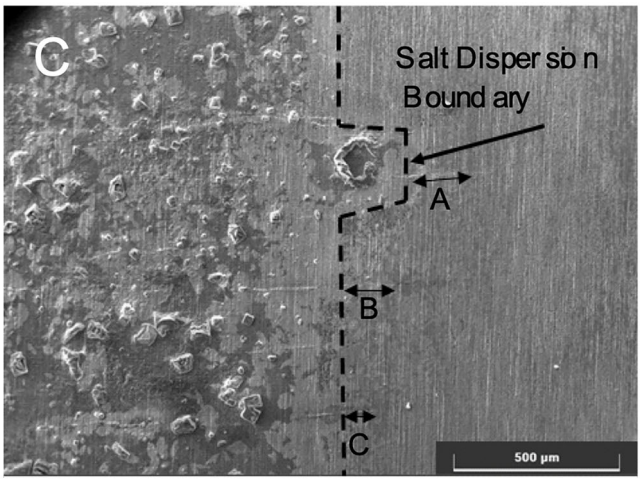


Fig. 8 | SEM images demonstrating. A standardized spacing between long cracks, which agrees with simulation results **B**, example of long cracks, and **C** positioning of the salt dispersion boundary and its role on total crack lengths. Some cracks are highlighted in red for better understanding.

shows the area of salt dispersion reported in Table 1. This figure demonstrates that a higher salt flux has a salt diffusion halo (seen as white contrast) three times as large as that for the lowest flux. Since crack size is not affected (or only marginally longer) with increasing flux, the fluxes employed seem

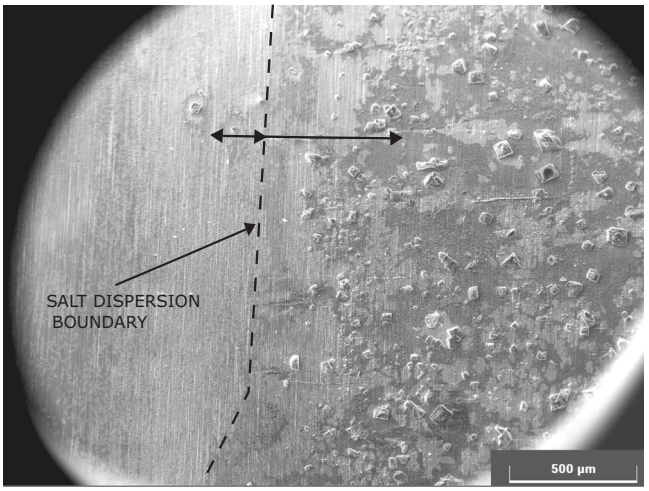


Fig. 9 | An example of an SEM image, which shows crack propagation quickly stagnating after passing the salt dispersion boundary.

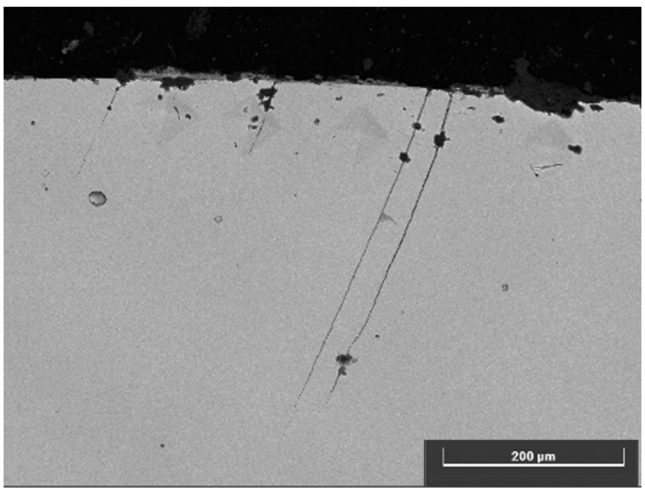


Fig. 10 | A through thickness microscopy image to show crack depths for a salted section of the c-ring.

to have a secondary effect on cracking. However, we can expect that for lower fluxes, the contaminant diffusion could be shorter than the cracks observed here and can limit cracking.

To further assess the previous findings, we considered the effect of salt patterns under fatigue loading. Hence, a corrosion-fatigue test was designed using notched samples with the same material (CMSX-4), closely following the design of the "Dot" test. This test followed the standard procedures previously used for corrosion-fatigue[20] (Fig. 21), only changing the salt deposition pattern. A micropipette deposited a droplet of salt solution (with a flux of 1.2 µg/cm^2/h) close to the notch center, as highlighted in Fig. 15. Note that this was only done on one of the two lateral notches and was followed by fatigue loading. An environment exposure of 300 ppm of SO_2 was used, and the specimen was now heated to a temperature of 700 °C, 150 °C higher than the C-ring tests. A strain-controlled tensile load was used to maintain a nominal load of 680 MPa and the specimen underwent cyclic loading with a 1-120-1-1 s trapezoidal loading pattern. This means a 1 s ramp up, 120 s dwell time, 1 s ramp down, and finally, a 1 s hold with no stress is applied (as shown in Fig. 20) until failure.

The results in Fig. 17 demonstrate that under cyclic loading, a localized salt deposition that prevents crack interactions significantly reduces the sample life. The "dot" specimen failed within 1505 cycles after reaching a crack depth of 1.9 mm, as shown in Fig. 16. Figure 17 also presents the

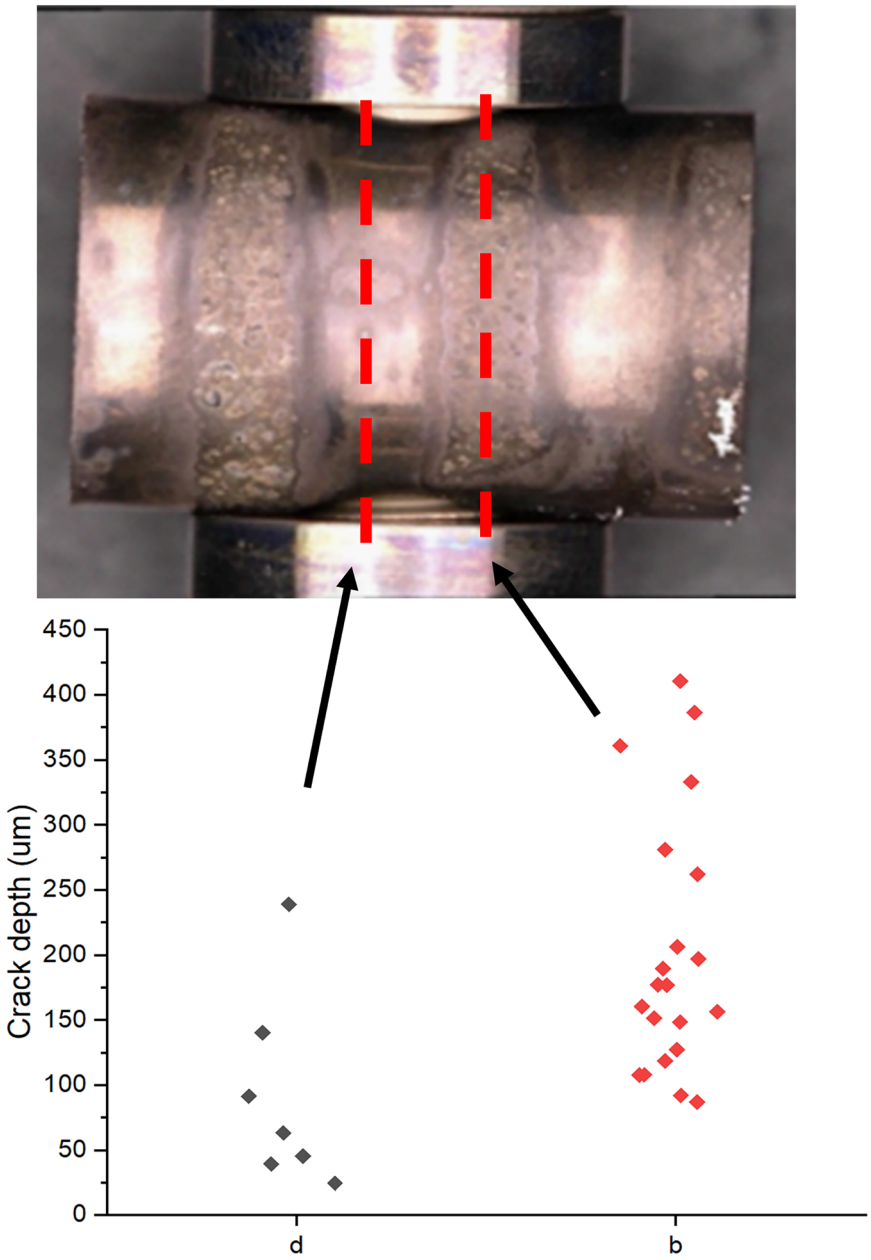


Fig. 11 | A plot to visualize the number of observed cracks and their respective depths for both a salted and an unsalted cross section.

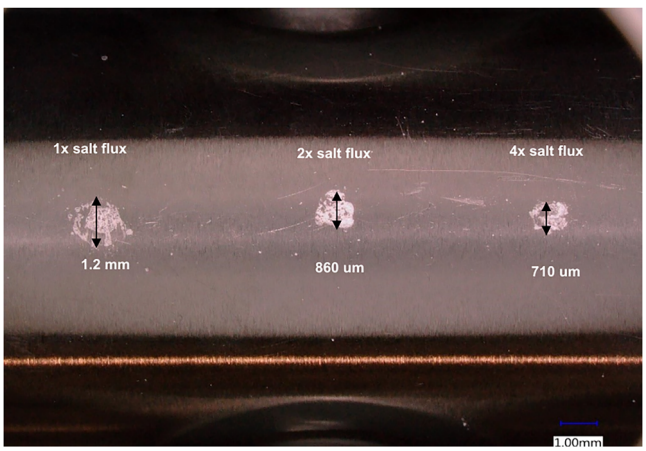


Fig. 12 | a Optical image showing the distribution of salt droplets for the pre-tested "One-Dot" C-ring.

results for three other equivalent tests, for which standard spray deposition method was used to fully coat the notch. Moreover, these samples required resalting (highlighted by the orange circles in Fig. 17) every 2000 cycles to achieve failure. These samples experienced a spike in the crack growth rate (CGR) after the resalting process due to the production of fresh crack embryos within a critical separation distance needed to encourage crack coalescence. The spike in CGR eventually plateaus once again, driven by further crack shielding mechanisms.

Overall, the "Dot" test halved the life of the test compared to the next most damaging test and resulted in an 83% decrease in life compared to the best prior test. More strikingly, none of the prior tests would have failed without resalting, which was not necessary for the "Dot" deposition. These results further support that the contamination pattern interacts with the number of initiation sites to promote or minimize shielding effects. As the "Dot" test provides only one location for potential embryos to initiate, it eliminates the probability of any interaction mechanisms occurring.

Prior work[10,15,21] has shown that the presence of solid NaCl particles in an SO_x environment drastically accelerates crack initiation in Ni superalloys

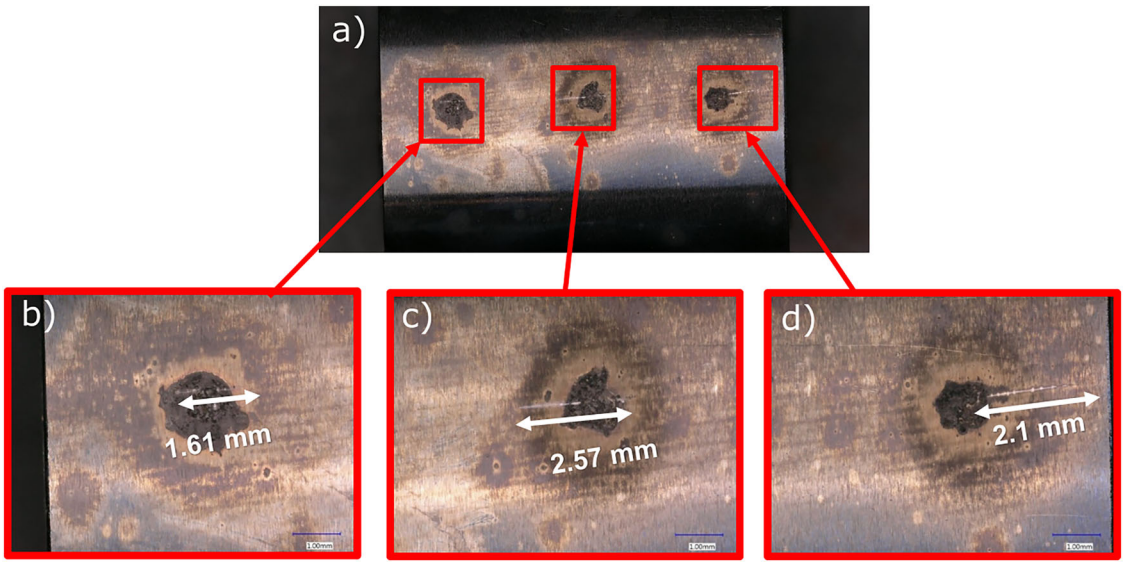


Fig. 13 | Optical images post testing of a C-ring with localized salt deposits. a Presents an overview to show the extent of cracking for each site of varying salt concentration while **b**, **c** and **d** representing 1x, 2x, and 4x salt flux respectively.

Fig. 14 | SEM images of the 'Dot' sample after testing. a-**c** Corresponds to varying salt flux (1.2 µg/cm2/h, twice, and four times as much respectively). The analysis demonstrates that as salt flux increases the area of salt dispersion also increases.

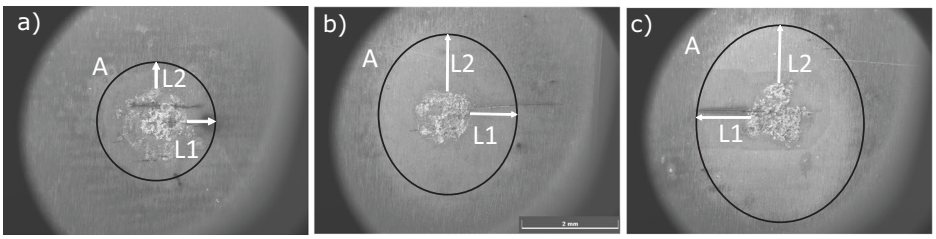


Table 1 | Measurements of final salt dispersion post-experiment for the increasing salt flux values, highlighting this increase in total area as the flux increases

Measurement	Fig 14a	Fig14b	Fig14c
L1 (mm)	0.44	1.45	1.53
L2 (mm)	0.34	1.32	1.59
Area (mm^2)	4.15	10.68	11.28

at intermediate temperatures. A chain of chemical reactions results in a sharp localized reduction of toughness, which leads to the initiation of embryos under the halos of salt particles. While these studies highlight the critical role of chemical interactions in crack formation, they do not consider how spatial distribution or density of salt affects crack interactions. This is a notable gap, particularly when prior work in non-corrosive environments have demonstrated that the spacing and density of cracks themselves can significantly influence their growth and coalescence behavior[22–24].

The problem involves multiple length and time scales and mechanisms that compete through the test. Not extensively, cracking is determined by the number of initiation sites, the diffusion of contaminants, the temperature, the available time, and the applied stress. In fatigue and creep-fatigue studies on Ni-based superalloys, closely packed cracks are known to interact via their plastic zones, leading to coalescent depending on loading conditions[23,25,26]. These findings emphasize the importance of both spatial and microstructural factors in dictating crack growth behavior. In addition, the rapid degradation suggests that the mechanism is not driven by bulk diffusion. Thus, a similar response would be expected for polycrystalline material, probably with more tortuous crack paths, but equally dominated by crack nucleation and interaction spacing.

The development of a digital twin of the experiments compared competing mechanisms and demonstrated that cracks can grow unbound if they are free from interacting with other cracks. Thus, this analysis suggested that the density, distribution, and pattern of contaminants determine the component reliability. In addition to explaining failure mechanisms, simulations have been instrumental in developing more accurate novel experimental protocols. The so-called Zebra and Dot deposition patterns effectively mitigated the likelihood of crack interactions and resulted in significantly more damaging conditions, with longer cracks and lower lives. This outcome is consistent with studies that have shown isolated cracks grow longer when unimpeded by neighboring cracks[22,25] and supports the hypothesis that engineered spacing of contaminants can control crack interaction behavior.

The integration of a digital twin that integrated all the available experimental data provided the understanding to mitigate some of the epistemic experimental uncertainty. In this case, crack lengths depend on the reduction of the local stress, which is a magnitude that cannot be measured directly and has large experimental uncertainty (the exception being exceptionally rare synchrotron techniques). Instead, simple elastic models could predict the local stress with lower uncertainty by mimicking the local crack configuration. This strategy effectively discerns mechanical from chemical crack growth drivers while the integration of models and experiments mitigates the overall uncertainty.

We highlight that this work has implications beyond superalloys and gas turbine applications. Offshore structures, which are heavily exposed to corrosive species, might benefit from isolating a salt deposition in testing to assess its response to different salt deposition patterns. Lower operating temperatures will affect crack initiation and propagation mechanisms, and

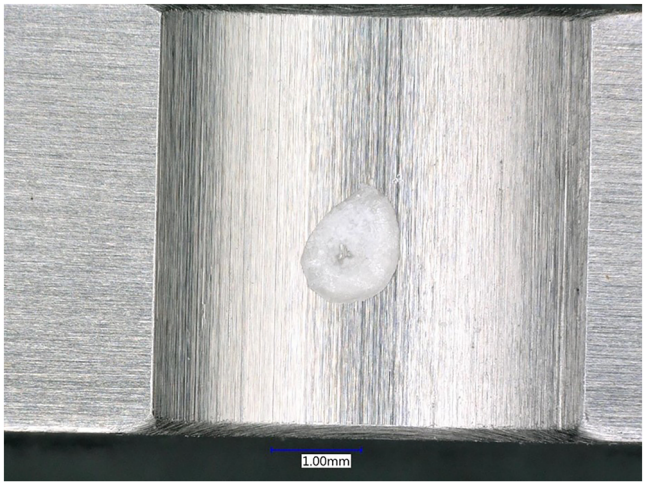


Fig. 15 | An optical image to show the singular droplet of salt solution being placed at a central point along the notch of a CMSX-4 fatigue specimen.



Fig. 16 | An optical image showing the crack surface morphology upon complete failure of the CMSX-4 fatigue specimen after 1505 cycles.

by testing different salt deposition patterns and densities, a better understanding of such mechanisms can be achieved. Hence, this work provide a strategy to engineers to understand the effects of contaminant deposition patterns and their effect on cracking under fracture and fatigue.

To summarize, this study integrates computational and experimental approaches to demonstrate that contamination patterns can have a notable effect on the cracking response of materials. We demonstrated that isolated local salt deposition can drastically accelerate cracking under detrimental environments that promote multiple crack embryos. A PFM correctly predicted that an isolated crack can reach lengths over 2 mm for a 50-h C-ring test under SO_2 environment. This crack is significantly longer than those physical C-ring tests under the same experimental conditions, which saw cracks propagate to lengths of 300 μm when salt depositions are not isolated. This result suggests salt patterns interact with the cracking mechanisms.

A "Zebra" salt pattern showed an overall increase in cracking, some reaching lengths more than 2× those previously seen. When salt droplets were isolated further in the "One-Dot" test cracks propagated in the range of 1.61 and 2.57 mm under static loading conditions. Additional fatigue testing demonstrated that a singular deposition spot drastically reduced the number of cycles to failure by as much as 83%. The analysis further suggests that the mechanical rather than diffusion length scales control crack growth. Further testing with different salt concentrations can clarify these effects.

Finally, this study exemplifies the benefits of integration of computational modeling and experiments to advance the understanding of complex problems by mitigating the largest uncertainties. Integrated approaches can better inform the entire research process, as they result in a deeper multi-dimensional understanding of problem.

Methods

Phase field models (PFM)[27–29] were proposed to describe the transition between two phases with a smooth continuous solution. In this work, the transition corresponds to a smooth degradation between uncracked and cracked material, as opposed to the more traditional sharp transition. This is illustrated by considering a damage parameter ϕ, which represents undamaged ($\phi = 0$) or fully damaged ($\phi = 1$) material[30] and depicted in Fig. 18.

PFM follows from Griffith's work[31] on fracture energy and proposes that crack propagation will occur when the critical energy release rate of the material, G_c, is degraded below a critical point. Degradation hence, depends on the mechanical solicitation of the system and the characteristic energy release rate, which is typically a function of material attributes such as composition and microstructure. Environmental conditions such as temperature and attack from embrittling contaminants also affect the material's energy release rate and they can be estimated following Eq. (1),

$$G_c(\theta) = G_c(0)(1 - \chi\theta) \tag{1}$$

in which $G_c(\phi)$ and $G_c(0)$ correspond to the critical energy release rates with and without the impact from embrittling contaminants, respectively, and χ is a degradation parameter that accounts for the role of contaminants in reducing the fracture energy. Furthermore, θ corresponds to the surface segregation coverage and can be estimated following the Langmuir–McLean model[32] (θ),

$$\theta = \frac{c * a}{(c * a) + (\frac{-\Delta G0}{RT})}, \tag{2}$$

for which where c is the contaminant concentration, "a" is a material parameter that controls the degradation gradient, G0 is the Gibbs free energy, R and T are the molar gas constant and temperature, respectively. The PFM[16] was implemented in the finite element software Abaqus 2022[33] using a User Elements (UEL) subroutine along with anisotropic elastic properties with cubic symmetry. Concentrations for corrosive impurities were allocated using the "temperature" degrees of freedom in Abaqus and a diffusivity parameter was supplied as user input to the model. Table 2 presents the model parameters. For further details about the formulation, implementation, and validation of this PFM, please refer to the previous study in ref. 16.

We consider standardized testing approaches such as ISO 7539-5[2] and ASTM G38[3]), which characterizes SCC using a C-shape sample shown in Fig. 19. The component consists of a partial circular section with holes on either side to allow a bolt, a nut and two washers to be placed. For this study, these C-rings are machined from CMSX-4[34], a single-crystal nickel superalloy, with the [001] crystal orientation parallel to the sectioned cylinder's geometric axis. The washer, bolt, and nut are machined from Waspalloy due to their resistance to corrosion and creep at high temperatures[35], and are known to minimize any stress relaxation effects on the C-ring. The composition of CMSX-4 is represented in Table 3.

The bolt is tightened to produce a predicted tensile stress distribution, which for this study has a peak value of ~700 MPa according to the methodology used in Duarte et al.[5], however, the value and positioning of the peak values depends both on the anisotropic nature of the material and the total displacement value of the bolt. The C-ring is first cleaned with isopropyl

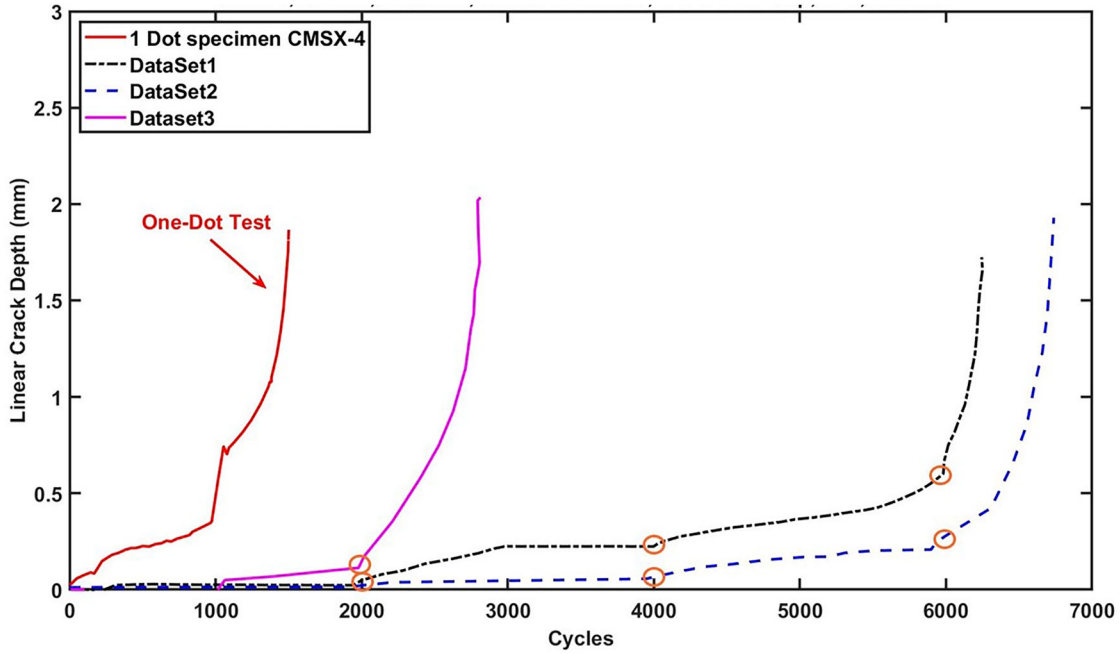


Fig. 17 | Plot highlighting the number of cycles needed to reach failure for a CMSX-4 corrosion-fatigue test, with the "One-Dot" test indicated by the red line. Please note that the 1-Dot test was NOT re-salted every 2000 cycles, unlike the other tests, which are highlighted using the orange circles.

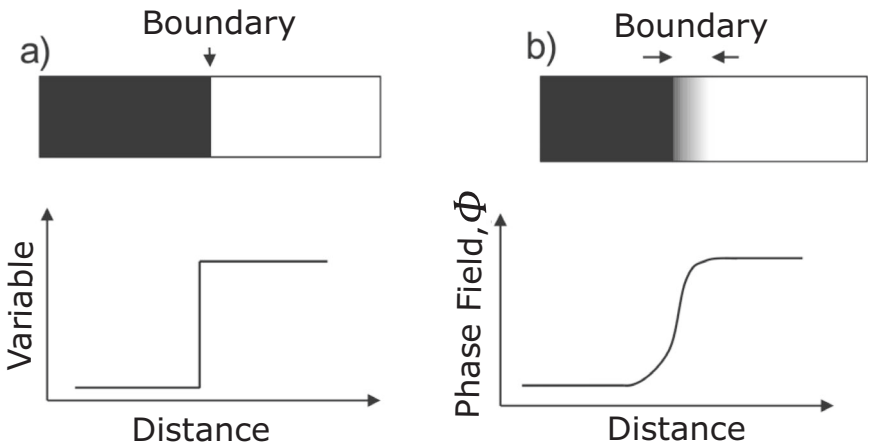


Fig. 18 | Smooth interface principle behind PFM. Boundary between phases for **a** sharp interface and **b** diffusive interface, highlighting the smooth transition used in PFM.

Table 2 | Values of the input parameters used for PFM corresponding to CMSX-4 at intermediate temperatures[16]

Parameter	Value
Young's modulus (GPa)	110.460
Poisson's ratio (ND)	0.3858
Shear modulus (GPa)	114.600
$G_c(0)$	40
Initial concentration (wmmp)	0.5
Temperature (°C/K)	540/813
Molar gas constant (N mm/(mol K))	8314.5
Gibbs free energy (kJ/mol)	-30
χ	0.998
Steepness parameter "a"	1.25

alcohol and in an ultrasonic cleaning tank, before being heated on a hot plate to the desired temperature. The NaCl, which is dissolved in deionised water to create a solution, is deposited onto the top surface using a spraying method before the C-ring is heated to evaporate any excess water. The sample is weighed before and after salting, and this deposition process is repeated until a desired salt flux is reached. The C-rings are then placed into a furnace at a predetermined temperature and time, where a gaseous environment, consisting of 300 ppm of SO_2, is introduced. This combination of salt and gas atmosphere is selected as it is known to activate SCC at 450–550 °C. The tests are run for either 15 min, 2-, 50-, or 400-h, and where necessary are generally resalted every 50 h.

Corrosion-fatigue testing corresponds to a double-notched fatigue specimens, which in the case of this study were machined from CMSX-4 and were cast in the ⟨001⟩ direction. The fatigue specimen is also cleaned with isopropyl alcohol and in an ultrasonic cleaning tank, before being heated on a hot plate to the desired temperature. As with the monotonic C-ring testing, the NaCl is dissolved in deionised water to form a solution, and the same

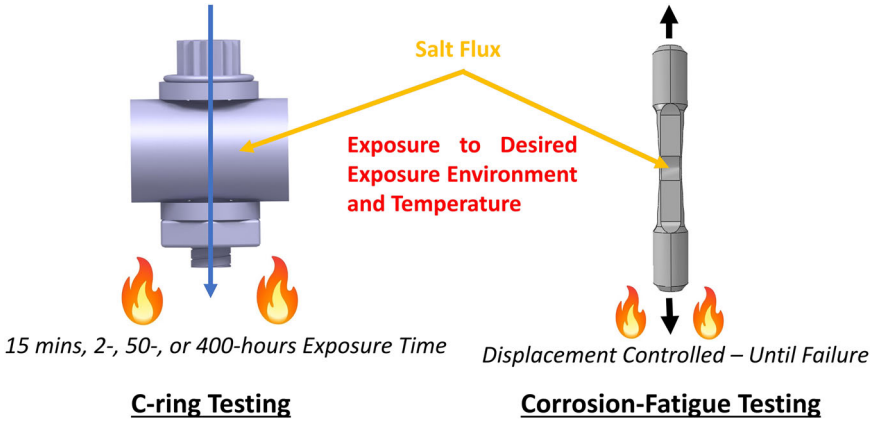


Fig. 19 | C-ring geometry with and without the bolt.

Table 3 | Composition of CMSX-4 (wt%)

Ni	Cr	Al	Co	Ta	W	Mo	Ti	Re	Hf
Balance	6.5	5.6	9.0	6.5	6.0	0.6	1.0	3.0	0.1

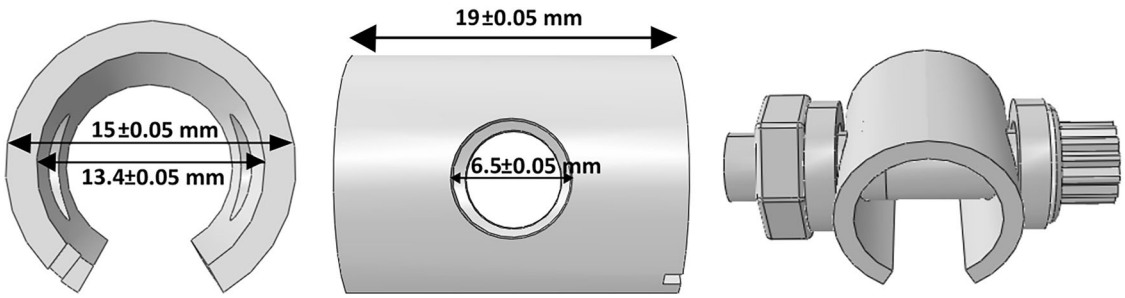


Fig. 20 | A schematic to represent the trapezoidal loading waveform used in all corrosion-fatigue experiments referred to in this thesis.

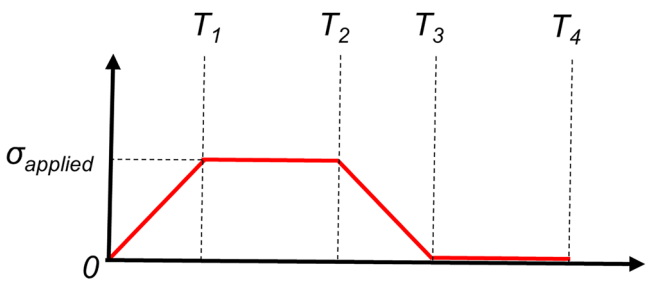


Fig. 21 | Schematic representing the experimental setups for both C-ring and corrosion-fatigue experiments used to recreate the corrosive environment of a gas turbine.

spraying method is used to coat one of the two notches. The sample is then heated to evaporate any excess water. When the desired weight of salt is achieved, the specimen is loaded into the corrosion-fatigue test rig, where several test parameters (including temperature, gaseous environment, and nominal load) are amended to simulate the desired environment. Trapezoidal loading waveforms are used, and is summarized in Fig. 20 where T1 is the time to increase to maximum load; T2 is the dwell time for which the maximum applied load is held; T3 is the time to decrease back to minimum load; and finally, T4 is the time for which the minimum load is maintained. The tests carried out are displacement-controlled and run until failure, with some tests being resalted at regular intervals. The experimental setups for both the C-ring and corrosion-fatigue tests are depicted in Fig. 21.

Data availability

Data supporting this study cannot be made available due to commercial and intellectual property restrictions.

Received: 25 January 2025; Accepted: 18 July 2025;
Published online: 10 August 2025

References

1. Raja, V. S., Cui, B. & Shoji, T. *Stress Corrosion Cracking: Theory and Practice* (Elsevier, 2025).
2. ISO 7539-2:1989 *Corrosion of Metals and Alloys-Stress Corrosion Testing-Part 2: Preparation and Use of Bent-Beam Specimens* (ISO, 1989).
3. Standard, A. et al. *Standard Practice for Making and Using c-ring Stress-Corrosion Test Specimens. ASTM G38-73 (Reapproved 1990)* (ASTM, 2007).
4. Standard Test Method for Determining Susceptibility to Stress-Corrosion Cracking of 2XXX and 7XXX Aluminum Alloy Products. https://doi.org/10.1520/G0047-20
5. Duarte Martinez, F. et al. Investigation into the effects of salt chemistry and SO_2 on the crack initiation of CMSX-4 in static loading conditions. In *Superalloys* 753–762 (Springer, 2020).
6. Gowreesan, V. & Grebinnyk, K. *Stress Corrosion Cracking in Steam Turbine: Two Case Studies* (American Society of Mechanical Engineers, 2017).
7. Ramírez, E. I. et al. Stress corrosion cracking of the slip-ring connectors of a 2 MW wind turbine. *Eng. Fail. Anal.* **141**, 106732 (2022).

8. Cheng, Y. F. *Stress Corrosion Cracking of Pipelines* (Wiley, 2013).
9. Li, R.-Z. et al. Effect of hot corrosion on cycle deformation and fracture behavior of Ti-6Al-4V alloy under salt coating. *Corros. Sci.* **224**, 111545 (2023).
10. Duarte Martinez, F. *Investigation into the Environmental Assisted Crack Initiation Mechanism of CMSX-4 in Simulated Aero Engine Environments at 450–550* °C. Ph.D. Thesis, Cranfield University (2022).
11. Joseph, S., Lindley, T. C., Dye, D. & Saunders, E. A. The mechanisms of hot salt stress corrosion cracking in titanium alloy Ti-6Al-2Sn-4Zr-6Mo. *Corros. Sci.* **134**, 169–178 (2018).
12. Sedlaček, M., Guštin, A. Z. & Žužek, B. Influence of laser surface texturing sequence on fatigue properties of coated cold work tool steel. *Metals* **10**, 1636 (2020).
13. Mi, N., Ghahari, M., Rayment, T. & Davenport, A. J. Use of inkjet printing to deposit magnesium chloride salt patterns for investigation of atmospheric corrosion of 304 stainless steel. *Corros. Sci.* **53**, 3114–3121 (2011).
14. He, W. et al. Droplet size-dependent localized corrosion evolution of m50 bearing steel in salt water contaminated lubricant oil. *Corros. Sci.* **208**, 110620 (2022).
15. Duarte Martinez, F. et al. Effect of NaCl and SO_2 on the stress corrosion cracking of CMSX-4 at 550 °C. *Mater. High Temp.* **0**, 1–13 (2023).
16. Elsherkisi, M., Martinez, F. D., Mason-Flucke, J., Gray, S. & Castelluccio, G. M. Interaction of stress corrosion cracks in single crystals Ni-base superalloys. *Eng. Fract. Mech.* **298**, 109899 (2024).
17. Han, Z., Qian, C., Tang, L. & Li, H. Determination of the enhancement or shielding interaction between two parallel cracks under fatigue loading. *Materials* **12**, 1331 (2019).
18. Lomaev, I. L. et al. On the mechanism of sulfur fast diffusion in 3-D transition metals. *Acta. Mater.* **67**, 95–101 (2014).
19. Carlsson, J. & Isaksson, P. Crack dynamics and crack tip shielding in a material containing pores analysed by a phase field method. *Eng. Fract. Mech.* **206**, 526–540 (2019).
20. Brooking, L., Gray, S., Sumner, J., Nicholls, J. R. & Simms, N. J. Interaction of hot corrosion fatigue and load dwell periods on a nickel-base single crystal superalloy. *Int. J. Fatigue* **117**, 13–20 (2018).
21. Mahobia, S., Sinha, P. K. & Ray, A. K. Influence of NaCl on high temperature corrosion and fatigue life of In718 superalloy. *J. Alloys Compd.* **672**, 181–189 (2016).
22. Pilchak, A. L. & Juhas, M. C. Microstructural effects on fatigue crack growth in waspaloy. *Metall. Mater. Trans. A* **37**, 3009–3019 (2006).
23. Jiang, R., Wang, J. & Liu, Y. Fatigue crack initiation and growth in Ni-based superalloys under thermo-mechanical loading. *Acta. Mater.* **87**, 1–12 (2015).
24. Qin, S., Zhao, X. & Chen, Y. Molecular dynamics simulations on crack spacing in Ni-based superalloys. *RSC Adv.* **14**, 8562–8571 (2024).
25. Jiang, Y., Sun, X. & Li, M. Fatigue crack growth in single-crystal Ni superalloy: role of orientation and microstructure. *Mater. Sci. Eng. A* **712**, 1–9 (2018).
26. Mohammed, I., Patel, T. & Reed, R. C. Crack coalescence and failure in RR1000 under thermo-mechanical fatigue. *Mater. Sci. Eng. A* **829**, 142177 (2022).
27. Zhuang, X., Zhou, S., Huynh, G., Aerias, P. & Rabczuk, T. Phase field modelling and computer implementation: a review. *Eng. Fract. Mech.* **262,** 108234 (2022).
28. Moelans, N., Blanpain, B. & Wollants, P. An introduction to phase-field modeling of microstructure evolution. *Calphad* **32**, 268–294 (2008).
29. Qin, R. & Bhadeshia, H. Phase field method. *Mater. Sci. Technol.* **26**, 803–811 (2010).
30. Zhou, S., Zhuang, X., Zhu, H. & Rabczuk, T. Phase field modelling of crack propagation, branching and coalescence in rocks. *Theor. Appl. Fract. Mec.* **96**, 174–192 (2018).
31. Griffith, A. A. Vi. The phenomena of rupture and flow in solids. *Phil. Trans. R. Soc. Lond. Ser. A* **221**, 163–198 (1921).
32. McLean, D. *Grain Boundaries in Metals* 347 (Oxford University Press, 1957).
33. Smith, M. *Abaqus/CAE User's Manual Abaqus 6.11* (2009).
34. Wahl, J. B. & Harris, K. Improved 3rd Generation Single Crystal Superalloy CMSX-4® Plus (SLS)—a Study of Evolutionary Alloy Development (2018).
35. Xue, L. Laser consolidation-rapid manufacturing process for making net-shape functional components. *Adv. Laser Mater. Process. Technol. Res. Appl*. 461–505 (2018).

Acknowledgements

The authors are grateful for the support from EPSRC Doctoral Training Partnership UK. This data was generated under ATI program 113180.

Author contributions

M.E.: Software, Methodology Data curation, Analysis, Manuscript preparation, F.D-M.: Data curation, Analysis, J.M-F.: Supervision, Project administration, S.G.: Conceptualization, Methodology development, Funding acquisition, Manuscript preparation. G.M.C.: Conceptualization, Methodology development, Funding acquisition, Manuscript preparation.

Competing interests

The authors declare no competing interests.

Additional information

Correspondence and requests for materials should be addressed to Gustavo M. Castelluccio.

Reprints and permissions information is available at http://www.nature.com/reprints

Publisher's note Springer Nature remains neutral with regard to jurisdictional claims in published maps and institutional affiliations.

Open Access This article is licensed under a Creative Commons Attribution 4.0 International License, which permits use, sharing, adaptation, distribution and reproduction in any medium or format, as long as you give appropriate credit to the original author(s) and the source, provide a link to the Creative Commons licence, and indicate if changes were made. The images or other third party material in this article are included in the article's Creative Commons licence, unless indicated otherwise in a credit line to the material. If material is not included in the article's Creative Commons licence and your intended use is not permitted by statutory regulation or exceeds the permitted use, you will need to obtain permission directly from the copyright holder. To view a copy of this licence, visit http://creativecommons.org/licenses/by/4.0/.

© The Author(s) 2025



https://dspace.org/

Effect of salt deposition patterns on stress corrosion cracking

Elsherkisi, Mustafa; Duarte Martinez, Fabian; Mason-Flucke, Julian C.; Gray, Simon; Castelluccio, Gustavo M.

2025-08-10
Springer
https://doi.org/10.1038/s41529-025-00650-2
Elsherkisi M, Duarte-Martinez F, Mason-Flucke J, et al., (2025) Effect of salt deposition patterns on stress corrosion cracking. npj Materials Degradation, Volume 9, Issue 1, August 2025, Article number 104

Downloaded from a DSpace repository. https://dspace.org/